

**Science****Remotely Sensed Biological Production in the  
Equatorial Pacific**Daniela Turk, *et al.**Science* **293**, 471 (2001);

DOI: 10.1126/science.1056449

***The following resources related to this article are available online at  
www.sciencemag.org (this information is current as of April 27, 2009 ):***

**Updated information and services**, including high-resolution figures, can be found in the online version of this article at:

<http://www.sciencemag.org/cgi/content/full/293/5529/471>

This article **cites 28 articles**, 6 of which can be accessed for free:

<http://www.sciencemag.org/cgi/content/full/293/5529/471#otherarticles>

This article has been **cited by** 18 article(s) on the ISI Web of Science.

This article has been **cited by** 1 articles hosted by HighWire Press; see:

<http://www.sciencemag.org/cgi/content/full/293/5529/471#otherarticles>

This article appears in the following **subject collections**:

Atmospheric Science

<http://www.sciencemag.org/cgi/collection/atmos>

Information about obtaining **reprints** of this article or about obtaining **permission to reproduce this article** in whole or in part can be found at:

<http://www.sciencemag.org/about/permissions.dtl>

We turn now to the final part of our discussion of the electrical structure of COS dielectrics. Interface charge is recognized as a substantial problem for field-effect charge inversion in a transistor. Interface charge can completely screen the semiconductor from an applied field and even result in a discontinuity in dielectric displacement, as was the case for the ferroelectric field of BaTiO<sub>3</sub> crystals glued to germanium (13, 14). The thesis of our heteroepitaxial approach is that oxide dielectrics can be grown as monolithic single-crystal structures on semiconductors, tying up the dangling bonds that are typical of the amorphous SiO<sub>2</sub>/Si structure. This would in turn eliminate extrinsic interface charge and maintain continuity in dielectric displacement at the oxide/semiconductor interface. We used capacitance data (Fig. 4) to prove this point.

High-frequency (HF, 1 MHz) and low-frequency (LF, 10 Hz) capacitance data were taken from a 250 Å-thick BaTiO<sub>3</sub> film on *p*-type germanium (Fig. 4A). An expanded view of the data in the bias range where the germanium surface potential varies from zero to its value at the Fermi level is shown (Fig. 4B). We can extract the density of interface charge (our measure of interface perfection) from  $\Delta C$ ,  $C_{LF} - C_{HF}$  in this bias range (21).

The capacitance of the MOS capacitor can be broken down into its component parts  $C_{ox}$  and  $C_{Ge}$ , as identified in the equivalent circuit inset in Fig. 4A ( $C_{ox}$  is the specific capacitance of the BaTiO<sub>3</sub> film).  $C_{Ge}$  is dependent on the germanium surface potential, interface defect charge, and inversion charge. The hashed regions are the bias range where the field effect is “depleting” the oxide semiconductor interface of majority carrier charge and initiating the process of minority carrier charge inversion (the upward turn of  $C_{LF}$  in Fig. 4A is the signature of field-effect-driven electron-hole pair generation and charge carrier inversion in the underlying *p*-type germanium). Dielectric displacement via gate charge must overcome the screening effect of any interface-trapped charge before the germanium inversion charge can even respond.  $\Delta C$  in this depletion region provides a measure of any extra capacitance that might be associated with the charging dynamics of interface traps.

The electron-hole recombination rate in this depletion region is frequency-dependent, as is the rate at which electrons can move into and out of interface traps. The majority carrier electron-hole contribution to  $C_{Ge}$  can keep up at high frequencies, but electron trapping at the interface cannot. Therefore, by sweeping the frequency ( $\omega$ ) of the small signal ac gate voltage,  $dV_g(\omega)$ , the capacitance associated with interface trapped charge,  $C_{it}(\omega)$ , goes to zero as  $\omega \Rightarrow \infty$ . The contribution of interface charge can be separated.

The data for the determination of the interface trap density,  $D_{it}$ , are provided (Fig. 4B);  $D_{it} \propto \Delta C$ . As these data show,  $\Delta C$  and hence

trapped charge for our commensurate interface are negligible.  $D_{it}$  is indistinguishable from zero through the entire depletion region. We therefore observe a  $D_{it}$  value of  $<10^{10}/\text{cm}^2\text{-eV}$ ; to our measurement sensitivity, this is an electrically perfect interface. The flat band shift indicates a fixed positive oxide charge of  $10^{12}/\text{cm}^2$ : a value consistent with an error of 50 parts per million in the Ba/Ti ratio in the structure. Germanium inverts from its majority carrier *p*-type behavior to minority *n*-type behavior over a narrow 1-V range. A ferroelectric hysteresis is not detectable in the capacitance-voltage data, because the coercive field for BaTiO<sub>3</sub> is only 500 V/cm (26): This value of the coercive field would shift the flat band by less than 1 mV in this 250 Å film.

To our knowledge, this is the first demonstration of field-effect charge inversion for a gate oxide on germanium. Its basis is the generalization of our structure series  $(AO)_n(A'BO_3)_m$  and the atomic-level flexibility that this structure series gives us to manipulate physical and electrical structure in a MOS capacitor. The COS approach enables the formation of commensurate interface structures while maintaining continuity in dielectric displacement and systematic control of inversion charge. COS in a MOS device is applicable to silicon or germanium and to any silicon-germanium alloy. Moreover, it offers promise in support of emerging technologies such as ferroelectric lithography (27) and quantum computing (28, 29), in which interface defect charge must be controlled to values less than  $10^{10}/\text{cm}^2$ .

References and Notes

1. D. Kahng, M. M. Atalla, “Silicon-Silicon Dioxide Field Induced Surface Devices” (IRE Solid-State Device Research Conference, Carnegie Institute of Technology, Pittsburgh, PA, 1960).
2. G. Lucovsky *et al.*, *Appl. Phys. Lett.* **74**, 2005 (1999).
3. G. Lucovsky, J. C. Phillips, *Appl. Surf. Sci.* **166**, 497 (2000).

4. R. A. McKee, F. J. Walker, M. F. Chisholm, *Phys. Rev. Lett.* **81**, 3014 (1998).
5. G. E. Jellison Jr. *et al.*, *Appl. Opt.* **33**, 6053 (1994).
6. M. R. Melloch *et al.*, *Crit. Rev. Solid State* **21**, 189 (1996).
7. R. A. McKee *et al.*, *Appl. Phys. Lett.* **59**, 782 (1991).
8. R. A. McKee *et al.*, *Appl. Phys. Lett.* **63**, 2818 (1993).
9. These data are collected and discussed as supplementary Web material and can be found on Science Online at [www.sciencemag.org/cgi/content/full/293/5529/468/DC1](http://www.sciencemag.org/cgi/content/full/293/5529/468/DC1).
10. R. W. G. Wyckoff, *Crystal Structures 1* (Interscience, New York, 1951), chap. VII, section a5, and fig. VIIA, part 6a.
11. R. A. McKee, F. J. Walker, U.S. Patent 5,830,270 (1998).
12. ———, E. D. Specht, G. E. Jellison, L. A. Boatner, *Phys. Rev. Lett.* **72**, 2741 (1994).
13. D. H. Looney, U.S. Patent 2,791,758 (1957).
14. W. L. Brown, U.S. Patent 2,791,759 (1957).
15. N. Arora, *MOSFET Models for VLSI Circuit Simulation, Theory and Practice* (Springer-Verlag Wien, New York, 1993).
16. F. J. Walker *et al.*, in preparation.
17. S. A. Campbell *et al.*, *IEEE Trans. Electron. Dev.* **44**, 104 (1997).
18. M. Copel, M. Gribelyuk, E. Gusev, *Appl. Phys. Lett.* **76**, 436 (2000).
19. K. Eisenbeiser *et al.*, *Appl. Phys. Lett.* **76**, 1324 (2000).
20. J. R. Brews, *J. Appl. Phys.* **46**, 2181 (1975).
21. An excellent treatment of MOS dielectric theory and field-effect phenomena in such a device can be found in Nicollian and Brews (see p. 332 for discussion of  $D_{it}$  and  $\Delta C$ ) [E. H. Nicollian, J. R. Brews, *MOS (Metal Oxide Semiconductor) Physics and Technology* (Wiley, New York, 1982)].
22. J. Robertson, C. W. Chen, *Appl. Phys. Lett.* **74**, 1168 (1999).
23. J. Robertson, *J. Vac. Sci. Technol. B* **18**, 1785 (2000).
24. S. A. Chambers *et al.*, *Appl. Phys. Lett.* **77**, 1662 (2000).
25. R. A. McKee, F. J. Walker, unpublished data.
26. W. J. Merz, *Phys. Rev.* **95**, 690 (1954).
27. A. Lin *et al.*, *Appl. Phys. Lett.* **78**, 2034 (2001).
28. J. Levy, in preparation.
29. B. E. Kane, *Fortschr. Phys.* **48**, 1023 (2001).
30. J. Tershoff, *Phys. Rev. Lett.* **52**, 465 (1984).
31. We thank G. Ice, E. Specht, and J. Lettieri for careful review of and comments on our manuscript. Sponsored by the Division of Materials Sciences and Engineering, Office of Basic Energy Sciences, U.S. Department of Energy at Oak Ridge National Laboratory under contract DE-AC05-00OR22725 with UT-Battelle.

2 April 2001; accepted 18 June 2001

## Remotely Sensed Biological Production in the Equatorial Pacific

Daniela Turk,<sup>1,2\*</sup> Michael J. McPhaden,<sup>2</sup> Antonio J. Busalacchi,<sup>3</sup> Marlon R. Lewis<sup>1</sup>

A combination of ship, buoy, and satellite observations in the tropical Pacific during the period from 1992 to 2000 provides a basin-scale perspective on the net effects of El Niño and La Niña on biogeochemical cycles. New biological production during the 1997–99 El Niño/La Niña period varied by more than a factor of 2. The resulting interannual changes in global carbon sequestration associated with the El Niño/La Niña cycle contributed to the largest known natural perturbation of the global carbon cycle over these time scales.

Interannual fluctuations in the coupled climate system over the tropical Pacific Ocean may induce substantial variability in the global carbon cycle because of effects on biological production in this region (1–6). In par-

ticular, new production (7) is a critical element in this assessment (2), because it is the central engine of the biological carbon pump that, along with the solubility pump (8), maintains the gradient of dissolved inorganic

carbon between the surface and the deep ocean. Over long time scales, it should be equivalent to the carbon that is exported from the surface ocean (7). In recent years, fluctuations in new production have been evaluated at a limited number of locations in the equatorial Pacific (5, 6, 9–14); however, an evaluation of the net effect of El Niño–Southern Oscillation (ENSO) on the rates of new production over the entire equatorial band is lacking because of the spatial and temporal limitations of field observations. We have used a combination of a large number of ship observations, data from the Tropical Atmosphere Ocean (TAO) buoy (15), and TOPEX/Poseidon altimeter data (16) to quantitatively evaluate the interannual variability of new production in the entire equatorial Pacific band during the time period from 1992 to 2000, which includes the recent extreme 1997–98 El Niño and the strong 1998–99 La Niña (17). The resulting variation in the export of carbon during the 1997–99 period is of profound importance for the planetary carbon cycle, because carbon may be sequestered below the thermocline over time scales that are long in relation to the current atmospheric CO<sub>2</sub> transient.

Direct measurements of new production along the equator have suggested that interannual variation in new production in the western and central equatorial Pacific correlates well with changes in nutricline and thermocline depth during El Niño (3, 6), a result that is consistent with changes in phytoplankton pigment concentration associated with changes in sea level (18). This is a result of increases in the supply of nutrients into the

upper well-lit surface layer. Frequently, as a result of nutricline/thermocline shoaling, large variations in new production appear at depth below the upper surface mixed layer and do not have a signature in the surface pigment (6). Consequently, existing satellite approaches for deriving information about new production from surface color signatures, and an assumed ratio between new primary production and total primary production (*f* ratio) (7, 19), would result in large underestimates.

We have used observed relationships between sea level, thermocline depth, and new production to determine the basin-scale interannual variability of new production in the equatorial Pacific. We take advantage first of the spatial coverage of remotely sensed sea level afforded by the TOPEX/Poseidon altimeter to infer changes in the depth of the thermocline (20) and second, of a newly derived relationship between the thermocline depth and the vertically integrated rate of new production (21). These data clearly show that sea level is a robust indicator of thermocline movement in the equatorial Pacific (Fig. 1). The 10-day sea level anomalies and the 10-day 20°C depth anomalies are highly correlated with one another. The coefficient of determination, *r*<sup>2</sup>, is 0.86 and 0.85 in the western (145°E to 165°E) and eastern (165°W to 100°W) portions of the equatorial band, respectively, and 0.73 in the central region (165°E to 165°W). Possible reasons for relatively lower correlation in the central region may include the role of lateral advection and higher noise-to-signal ratio at the pivot point of the thermocline movement in this area. The average slope of the regression is 177 ± 3 (meters of thermocline displacement/meter of sea level adjustment, ±1 SE of the slope). These results are consistent with other recent observations of surface manifes-

tations of subsurface isopycnal displacement (22).

The relationship between the 20°C depth and integrated new production was first calculated for the same three geographical regions as above. The depth of the 20°C isotherm and integrated new production are well correlated in both the west (*r*<sup>2</sup> = 0.83) and east (*r*<sup>2</sup> = 0.50) and are out of phase spatially. In the west, the thermocline/nutricline shoals during El Niño and consequently new production rates increase, whereas in the east, the thermocline/nutricline is deeper during El Niño and new production declines (6). In the central Pacific, the relationship between the 20°C depth and new production resembles that observed in the western region during El Niño conditions and resembles that observed in the eastern region during non-El Niño conditions. After the pooling of all data from the entire equatorial Pacific band, the integrated new production and the depth of the 20°C isotherm (Fig. 2) are highly correlated (*P* < 0.001), with a slope of -0.015 ± 0.004 mmol of N m<sup>-3</sup> day<sup>-1</sup> and an intercept of 3.32 ± 0.63 mmol of N m<sup>-2</sup> day<sup>-1</sup> (±1 SE of the slope and intercept). We also considered an alternate model that included local wind stress in order to evaluate the importance of local upwelling. This model did not significantly improve the fit to the new production data because of the dominant role played by thermocline depth variations on interannual time scales in controlling vertical fluxes of heat and nutrients into the surface layer (23).

We used these relationships to calculate the interannual fluctuations of new production from TOPEX/Poseidon data over the entire equatorial band (140°E to 100°W, 1°N to 1°S) over the period 1992–2000. The resulting time series of new production in the equatorial Pacific exhibits pronounced inter-

<sup>1</sup>Department of Oceanography, Dalhousie University, Halifax, Nova Scotia, Canada B3H 4J1. <sup>2</sup>Pacific Marine Environmental Laboratory, National Oceanic and Atmospheric Administration (NOAA), 7600 Sand Point Way, Seattle, WA 98115-0070, USA. <sup>3</sup>Earth System Science Interdisciplinary Center, University of Maryland, College Park, MD 20742-2425, USA.

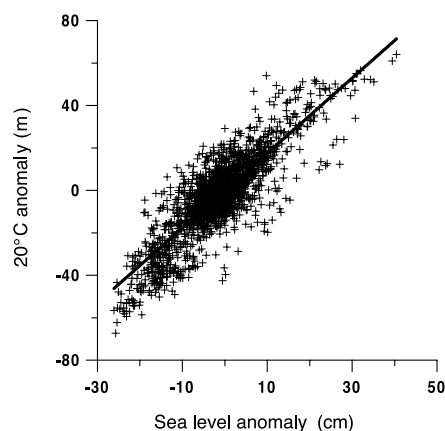


**Fig. 1.** Relationship between 10-day TOPEX/Poseidon sea level anomaly and TAO 20°C isotherm depth anomaly in the equatorial Pacific along the equator for 1992–2000.

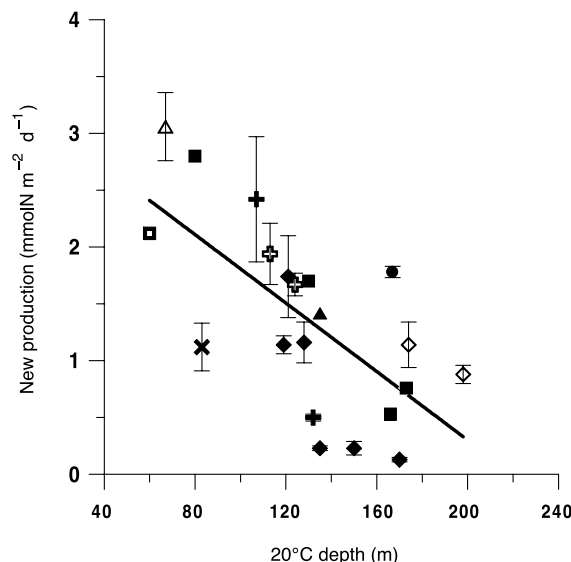


**Fig. 2.** Relationship between 20°C isotherm depth and vertically integrated new production in the equatorial Pacific; the solid and open diamonds are new production measurements averaged over 145°E to 165°E and 165°E to 165°W along the equator in the Warm Pool and Cold Tongue (6), respectively (±1 SE). Solid squares (5), open squares (9), open triangles (10), solid crosses (11), open diamonds (33), solid triangles (12), solid circles (13), and x's (14) are published averages from 1°N to 1°S (±1 SE) from various locations and time periods (21).

## REPORTS

annual variability (Fig. 3). During El Niño conditions, new production increases in the west and decreases in the east as a result of the change in nutrient supply associated with variations in the depth of the thermocline. This result is consistent with recent observations of the influences of thermocline uplift and biomass changes over the global ocean associated with Rossby waves (24), mesoscale upwelling in subtropical gyres (22), and tropical instability waves near the equator (25, 26). The net effect over the equatorial Pacific is a reduction of new production during El Niño and an increase during La Niña (Fig. 4), due to the dominance of the eastern equatorial Pacific in the new production dynamics.

The 1997–98 El Niño, by some measures the strongest on record, was followed by the strong 1998–99 La Niña. The consequences for the biological productivity of the equatorial Pacific region were substantial, resulting in a decrease of 30% in the export of carbon from the mean state over the equatorial Pacific during the 1997–98 El Niño and an increase of 40% during the 1998–99 La Niña. Our estimate of the mean areal new production in the equatorial Pacific outside of either the El Niño or La Niña periods ( $1.8 \pm 0.4$  mmol of N  $m^{-2} day^{-1}$ ) is comparable to that computed independently from estimated total primary production and an assumed  $f$  ratio in the eastern and central Pacific [table 1 in (5);  $1.7$  mmol of N  $m^{-2} day^{-1}$ ]. However, the reduction associated with El Niño and the increase due to La Niña are smaller than that computed for these regions alone (5). This is because of our inclusion of the western Pacific, where the out-of-phase thermocline tilting between west and east moderates the amplitude of the derived response averaged over the entire basin. If we accept previous estimates of the contribution of the equatorial Pacific to global oceanic carbon export (2) (10 to 56%), then the amplitude of the El Niño/La Niña cycle imposes a variation of 3 to 22% in the amount of carbon lost from the global surface ocean.

Our conclusions with respect to variations in new production are consistent with satellite observations of changes in phytoplankton pigment that clearly demonstrate the transition from El Niño to La Niña conditions in the central equatorial Pacific (27). Although there are no direct measurements of new production during this time when the thermocline was shoaling, the increase in pigment in early 1998 is an unequivocal manifestation of increased new production. In addition, our estimates of interannual variations in new production correspond closely to independent estimates of the vertical volume transports in the thermocline, estimated for the region from  $8^{\circ}N$  to  $8^{\circ}S$  and  $156^{\circ}E$  to  $95^{\circ}W$  during 1992–2000 from TAO and Expendable

Bathythermograph temperature data and from wind stress estimates by the European Center for Medium Range Weather Forecasts (28). This correspondence adds further confidence to our conclusion that vertical fluxes regulate the supply of nutrients into the euphotic zone in the equatorial Pacific, and therefore govern new production, on ENSO time scales.

Previous studies have suggested that biological production and phytoplankton biomass in the eastern equatorial Pacific are limited by iron (29) or silicate (30) rather than by nitrate. However, in the eastern Pacific, iron and silicate input are largely a

result of vertical fluxes, so that iron, silicate, and nitrate inputs are correlated in the vertical. Thus, although the proximate limitation of new production might be iron or silicate rather than nitrate input (29), our conclusions regarding the relationship between new production and thermocline depth as estimated from satellite altimetry will be unaffected.

The analysis presented here permits the estimation of key processes in the ocean carbon cycle on synoptic scales in the equatorial Pacific, by taking advantage of the spatial coverage provided by remotely

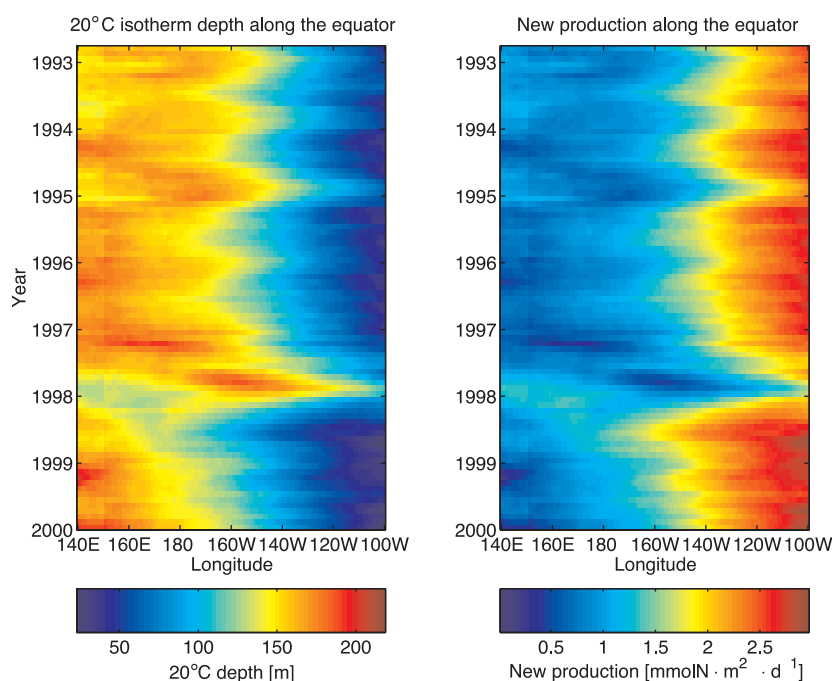


**Fig. 3.** Monthly time/longitude sections of 20°C isotherm depth and new production along the equator (from 140°E to 100°W) for 1992–2000.

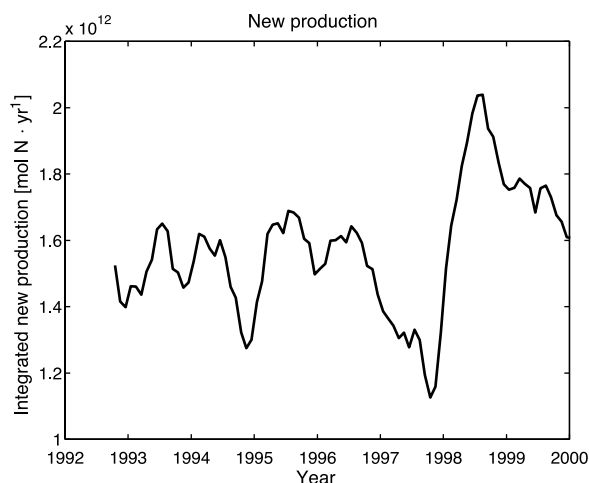


**Fig. 4.** Monthly time series of new production in the equatorial band integrated from 140°E to 100°W,  $1^{\circ}N$  to  $1^{\circ}S$ , for the time period 1992–2000. The estimated error in the prediction of monthly new production, determined by propagation of uncertainties in the prediction of derived thermocline depths and uncertainties in prediction of new production from thermocline depths, is  $0.4$  mmol of N  $m^{-2} day^{-1}$ , or about 25% of the mean value.

sensed observations together with a transfer function derived from in situ observations. The net basin-integrated effect of El Niño and La Niña events on the rates of biological production in the equatorial Pacific is significant and plays a strong role in the largest known natural year-to-year perturbation of the global carbon cycle (5, 25, 37). Future observations will provide data to validate the approach on larger spatial scales, extending it to off-equatorial regions and possibly to global scales.

References and Notes

1. R. T. Barber, F. P. Chavez, *Science* **222**, 1203 (1983).
2. F. P. Chavez, R. T. Barber, *Deep-Sea Res.* **34**, 1229 (1987).
3. R. T. Barber, J. E. Kogelschatz, in *Global Ecological Consequences of the 1982-83 El Niño-Southern Oscillation*, P. W. Glynn, Ed. (Elsevier, New York, 1989), pp. 21–53.
4. J. W. Murray, R. T. Barber, M. R. Roman, M. P. Bacon, R. A. Feely, *Science* **266**, 58 (1994).
5. F. P. Chavez et al., *Science* **286**, 2126 (1999).
6. D. Turk, M. R. Lewis, W. G. Harrison, T. Kawano, I. Asanuma, *J. Geophys. Res.* **106**, 4501 (2001).
7. R. W. Eppley, B. J. Peterson, *Nature* **282**, 677 (1979).
8. R. A. Feely, R. Wanninkhof, T. Takahashi, P. Tans, *Nature* **398**, 597 (1999).
9. J. W. Murray, J. N. Downs, S. Storm, C. L. Wei, H. W. Jannasch, *Deep-Sea Res.* **36**, 1471 (1989).
10. M. A. Peña, M. R. Lewis, W. G. Harrison, *Mar. Ecol. Prog. Ser.* **80**, 265 (1992).
11. J. J. McCarthy, C. Garside, J. L. Nevins, R. T. Barber, *Deep-Sea Res.* **43**, 1065 (1996).
12. M. Rodier, R. LeBorgne, *Deep-Sea Res.* **44**, 2085 (1997).
13. P. Raimbault et al., *J. Geophys. Res.* **104**, 3341 (1999).
14. F. P. Wilkerson, R. C. Dugdale, *J. Geophys. Res.* **97**, 669 (1992).
15. M. J. McPhaden et al., *J. Geophys. Res.* **103**, 14169 (1998).
16. J. Picaut, A. J. Busalacchi, in *Radar Altimetry*, L. Fu, A. Cazenave, Eds. (Academic Press, New York, in press).
17. M. J. McPhaden, *Science* **283**, 950 (1999).
18. C. L. Leonard, C. R. McClain, *Int. J. Remote Sensing* **17**, 721 (1996).
19. P. Falkowski, R. T. Barber, V. Smetacek, *Science* **281**, 200 (1998).
20. The 20°C isotherm depth (a proxy for the thermocline depth) was determined from the TOPEX/Poseidon-derived sea surface height based on relationships established from the depth profiles of temperature collected by the TAO buoy array. The altimeter-derived sea level was binned into 10-day averages, with a spatial averaging of 1° × 1° degree. The depth of the 20°C isotherm was derived from eight buoys spread along the equatorial band, and these data were also averaged over the same 10-day interval as used for altimetric heights. The two data sets, covering a time period from 1992 to 2000, were matched with respect to time and space grids. Anomalies in sea level and 20°C depth were then obtained by subtracting the mean seasonal cycle of the sea level and 20°C depth, derived from the period 1993–1996, from the original time series (1992–2000). The mean formulated over this period is representative of the mean as determined from longer data sets of surface wind, sea surface temperature, and tide gauges (32). The depth of the 20°C isotherm across the entire equatorial domain (140°E to 100°W, 1°N to 1°S) for the period 1992–2000 was then calculated by adding the interannual anomalies as determined from TOPEX/Poseidon sea level anomalies to the mean state.
21. The values for depth-integrated new production and coincident thermocline depths were obtained from a variety of sources at different times and locations in the equatorial Pacific band from 1°N to 1°S. These

- included data from 145°E to 165°W during November–December 1994, December 1995–January 1996, January 1997, and December 1997–January 1998 (6); at 155°W for mean conditions, El Niño 1998 onset, El Niño 1998 maturity, and La Niña 1999 (5); at 87°W during June 1988 (9); at 135°W in April 1988 (10); at 140°W in February–March 1992 and August–September 1992 (11); at 167°E in October 1994 (12) (one reported station was removed from the analysis); at 150°W during November 1994 (13); at 150°W in February–March 1988 (14); and at 140°W in March 1992 and October 1992 [(33) with adjustments made in the day length for consistency with the other data]. New production was determined from shipboard measurements of <sup>15</sup>N-labeled nitrate, with the exception of (5), where we use reported primary production and the *f* ratio to determine the rates of new production.
22. D. A. Siegel, D. J. McGillicuddy Jr., E. A. Fields, *J. Geophys. Res.* **104**, 13359 (1999).
23. To evaluate the importance of local upwelling in our analysis, TAO data were used to compute zonal wind stress, assuming a constant drag coefficient (1.2 × 10<sup>-3</sup>) and air density. We calculated 10-day averages of the wind stress around the center dates of the new production data. The stresses were either averaged spatially over the same zonal intervals as the new production sections, or were computed at the longitude of new production data for values derived from a single location. The wind stresses were added to the regression of new production on thermocline depth in a stepwise fashion. The incremental improvement to the explained variance (4%) is not statistically different from zero. The reason for the relative lack of improvement when including local zonal wind stress is that large-scale, remotely wind-forced upwelling, as manifest through thermocline depth variations, is the principal physical process driving vertical fluxes of heat and nutrients into the surface layer, rather than local wind-forced upwelling. The primacy of non-local wind-forced dynamics in affecting large-scale thermocline depth variations and surface layer prop-

- erties is a common feature of most current theories of ENSO (34, 35).
24. B. M. Uz, J. A. Yoder, V. Osychny, *Nature* **409**, 597 (2001).
25. M. J. Behrenfeld et al., *Science* **291**, 2594 (2001).
26. The relative importance of other physical processes, such as meridional advection, local upwelling, salinity variations, and internal wave dynamics, will differ in areas outside the equatorial band. Based on recent observations, we anticipate that although the general form of our model will have wide applicability, the coefficients relating sea level to thermocline height and relating thermocline depth to new production may vary somewhat in different areas.
27. R. Murtugudde, S. Signorini, J. R. Christian, A. J. Busalacchi, C. R. McClain, *J. Geophys. Res.* **104**, 18351 (1999).
28. C. Meinen, M. J. McPhaden, *J. Phys. Oceanogr.*, **31**, 1324 (2001).
29. J. J. Cullen, *Limnol. Oceanogr.* **40**, 1336 (1995).
30. R. C. Dugdale, F. P. Wilkerson, *Nature* **391**, 270 (1998).
31. P. J. Rayner, I. G. Enting, R. J. Francey, R. Lagerfelds, *Tellus* **51B**, 213 (1999).
32. E. C. Hackert, A. J. Busalacchi, R. Murtugudde, *J. Geophys. Res.* **106**, 2345 (2001).
33. P. Wheeler, unpublished Joint Global Ocean Flux Study data (see <http://usjgofs.whoi.edu/jg/dir/jgofs/eqpac/>).
34. D. S. Battisti, *J. Atmos. Sci.* **45**, 2889 (1988).
35. P. S. Schopf, M. J. Suarez, *J. Atmos. Sci.* **45**, 549 (1988).
36. The authors are grateful to T. Mudge and D. McClurg for assistance with data processing and to C. McClain, I. Asanuma, and T. Kawano for insight and opportunities to pursue this research. Financial support was provided by NASA's Mission to Planet Earth Program, the Natural Sciences and Engineering Research Council of Canada, and NOAA's Office of Atmospheric and Oceanic Research.

10 October 2000; accepted 13 June 2001

# The Recent Increase in Atlantic Hurricane Activity: Causes and Implications

Stanley B. Goldenberg,<sup>1\*</sup> Christopher W. Landsea,<sup>1</sup> Alberto M. Mestas-Nuñez,<sup>2</sup> William M. Gray<sup>3</sup>

The years 1995 to 2000 experienced the highest level of North Atlantic hurricane activity in the reliable record. Compared with the generally low activity of the previous 24 years (1971 to 1994), the past 6 years have seen a doubling of overall activity for the whole basin, a 2.5-fold increase in major hurricanes (≥50 meters per second), and a fivefold increase in hurricanes affecting the Caribbean. The greater activity results from simultaneous increases in North Atlantic sea-surface temperatures and decreases in vertical wind shear. Because these changes exhibit a multidecadal time scale, the present high level of hurricane activity is likely to persist for an additional ~10 to 40 years. The shift in climate calls for a reevaluation of preparedness and mitigation strategies.

During 1970–1987, the Atlantic basin experienced generally low levels of overall tropical cyclone activity. The relative lull was manifested in major hurricane (*I*) activity (Fig. 1), major hurricane landfalls on the East Coast of the United States and overall hurricane activity in the Caribbean. A brief resurgence of activity in 1988 and 1989 made it

appear that the Atlantic basin was returning to higher levels of activity similar to the late 1920s through the 1960s (2). This notion was later discarded when the activity returned to lower levels from 1991–1994 (3), due in part to the long-lasting (1990–1995) El Niño event (4). This event ended in early 1995 and was followed later that year by one of the